Phase-field-crystal methodology for modeling of structural transformations

Michael Greenwood,[1,2] Jörg Rottler,[1] and Nikolas Provatas[2]

[1]*Department of Physics and Astronomy, University of British Columbia, 6224 Agricultural Road, Vancouver, BC, Canada V6T 1Z1*
[2]*Department of Materials Science and Engineering, McMaster University, 1280 Main Street West, Hamilton, Ontario, Canada L8S 4L7*

We introduce and characterize free-energy functionals for modeling of solids with different crystallographic symmetries within the phase-field-crystal methodology. The excess free energy responsible for the emergence of periodic phases is inspired by classical density-functional theory, but uses only a minimal description for the modes of the direct correlation function to preserve computational efficiency. We provide a detailed prescription for controlling the crystal structure and introduce parameters for changing temperature and surface energies, so that phase transformations between body-centered-cubic (bcc), face-centered-cubic (fcc), hexagonal-close-packed (hcp), and simple-cubic (sc) lattices can be studied. To illustrate the versatility of our free-energy functional, we compute the phase diagram for fcc-bcc-liquid coexistence in the temperature-density plane. We also demonstrate that our model can be extended to include hcp symmetry by dynamically simulating hcp-liquid coexistence from a seeded crystal nucleus. We further quantify the dependence of the elastic constants on the model control parameters in two and three dimensions, showing how the degree of elastic anisotropy can be tuned from the shape of the direct correlation functions.

I. INTRODUCTION

The properties of materials are controlled by microstructures that evolve in the material during thermal and mechanical processing. These microstructures can coarsen in time and create a network of defects and grains that ultimately depends on the elements of a material, bond strength, crystal symmetry, and the phase transformation kinetics that govern microstructure evolution. In metallurgical processes, metals typically form body-centered-cubic (bcc), face-centered-cubic (fcc), or hexagonal-close-packed (hcp)lattices. These lattice symmetries influence grain boundary energies, triple lines, junction points, as well as the motion of defects such as dislocations, which move through crystals and interact with each other and grain boundaries. These processes are exploited to improve the strength of metals.

Large-scale simulations of defect evolution in microstructure are challenging due to their interactions through long-range elastic fields. To accurately represent such a situation, a model must resolve features ranging from individual defects and their interactions to those large enough to incorporate multiple grains on the mesoscale. Two modeling schemes that have emerged for capturing these opposing levels of interaction are the phase field methodology [1–4] and molecular-dynamics simulations [5–7]. These two approaches have distinct advantages and limitations on large and small spacial and time scales.

Phase field methods are able to capture mesoscale structure and kinetics by washing out atomic-scale details. Order parameters are introduced to describe uniform bulk properties of phases and the free energy of interfaces between them. However, since atomic scale interactions are omitted, dislocations, crystal structure, and grain boundary structure are ignored. These effects can thus only be integrated into a phase field model through effective coefficients or additional fields [8–12]. At the other end of the spectrum, molecular dynamics (MD) explicitly incorporates atomic interactions through appropriate atomic potentials. A number of these potentials have been presented to reproduce atomistic and bulk properties of materials [13–15]. MD simulations make it possible to self-consistently capture elastic interactions, defects, and crystalline symmetries. However, since MD simulations must track all atoms on time scales of atomic vibrations, they are limited to very small spacial and time scales.

A third approach is classical density-functional theory (CDFT), which models atomic properties of liquids or solids using information from liquid state particle correlation functions [16–19]. At the heart of the CDFT formalism is a free energy written in terms of an atomic number density field. The free energy is typically expanded in a truncated functional series about a reference density, where the terms in the expansion represent contributions from different interparticle correlations. Implicit in CDFT is a temporal coarse graining that removes the time-scale limitation of molecular dynamics. On the other hand, CDFT resolves structure at the atomic scale through a continuum field, thus requiring sufficiently fine numerical meshes to resolve atomic features. As crystals in CDFT emerge from the liquid state, density peaks can become quite sharp, leading to prohibitively large memory requirements for practical simulations [20].

A simpler class of continuum atomic scale models are phase field crystal (PFC) models [21]. The PFC technique also incorporates atomic scale effects, such as elastoplasticity and polycrystalline grain boundary interactions [22–24]. At the heart of the PFC formalism is a free-energy density that is constructed to be minimized by periodic density states with the symmetries of crystal phases, a principle originally inspired by the periodic solutions of the Swift-Hohenberg equation [25]. It has been shown that PFC models arise naturally from CDFT by retaining only a crude approximation of the two-point correlation function and reference free energy that enters CDFT [26]. This type of simplification maintains only the salient features found in CDFT, but has the benefit of representing atoms as low-amplitude periodic modulations that are simple to simulate efficiently.

The free energy of the first PFC model for pure materials [21] was constructed in gradients of an order parameter n to fourth order, given by

$$\Delta F = \int d\vec{r}\{n[(q_o^2 + \nabla^2)^2 - \epsilon]n/2 + n^4/4\}, \qquad (1)$$

where the parameter q_o sets in the relevant length scale of the problem and ϵ shifts the energy between a single and double well, making possible transitions between periodic and constant phases. This minimal model was shown to capture elastic and plastic effects self-consistently while maintaining broad, low-amplitude density peaks [21,22,27,28]. The time evolution of a system described by this free-energy functional can be obtained from conservative dissipative dynamics,

$$\frac{\partial n(\vec{r})}{\partial t} = \vec{\nabla} \cdot \left(M\vec{\nabla}\frac{\delta \Delta F}{\delta n(\vec{r})} \right), \qquad (2)$$

where M is a kinetic mobility parameter [21]. Conserved noise can also be added to facilitate nucleation from metastable states [19,21]. For the case of a constant M, these dynamics can be efficiently evolved in reciprocal space using a semi-implicit technique [22,29]. This makes possible significantly larger simulation time steps than usual finite differencing. Including an extra inertial term in the time evolution of Eq. (2) also makes it possible to model quasi-instantaneous elastic relaxation [23].

With the free energy of the above PFC model, it is only possible to simulate simple crystal structures such as two-dimensional (2D) hexagonal and three-dimensional (3D) bcc lattices. While it has been shown that the 3D PFC free energy contains fcc and hcp phases [20,30], the energy difference between the phases may be too small to exhibit structural transformations [31], particularly in the presence of noise. It is also not possible to easily manipulate coexistence between the fcc, bcc, and liquid phases in a manner corresponding to real materials. A great deal of research in this area is presently focusing on the development of a methodology to expand the original PFC formalism to better control the physical parameters of PFC models and to simulate a broader range of crystal structures, all while maintaining the computational advantage of broad density peaks.

Jaatinen *et al.* [20] recently developed an eighth-order extension of the original PFC free energy that can be used to better fit the surface energy properties of bcc iron. The same work showed that a kernel strictly input from a CDFT functional leads to fcc crystals with numerically unmanageably sharp density peaks. Wu *et al.* [32–34] expanded upon the original PFC model [21] by including secondary modes in their correlation kernels, and succeeded to stabilize fcc (3D) and square (2D) lattices. The phase diagram produced this way, however, does not allow for structural transformation directly between the fcc and bcc crystals. We have recently developed a formalism for constructing multiple-mode correlation functions that allows triangular, square, simple-cubic (sc), bcc, and fcc lattices to be simulated efficiently [35]. Our approach gives rise to realistic materials phase diagrams that make it possible to conduct temperature quenches between various phases of various crystal structures (e.g., bcc-fcc transformation).

This paper further expands upon these ideas, showing how to produce multimode correlation function kernels that stabilize the major crystal symmetries of metals, and how these can be parametrized to independently tune anisotropy in the elastic modulus tensor (or the crystal-melt surface tension) in different phases. Section II introduces the new free-energy functional, showing how to construct peaks in its correlation kernel. This is achieved first by an examination of the local part of the free-energy functionals used in different PFC models. The second portion of this section analyzes the free-energy contribution of different modes of our correlation kernel, demonstrating how to stabilize a particular lattice. Section III details the construction of a phase diagram for a model system exhibiting structural transformations between fcc-bcc-liquid phases. We also show that our method can model an hcp-bcc-liquid system. Section IV characterizes the elastic coefficients for square and fcc phases, and shows how to tune the anisotropy in the elastic moduli.

II. FREE-ENERGY FUNCTIONAL

The PFC free-energy functional can be broken down into three components. First is a purely entropic local energy ΔF_{id} responsible for driving the system to a stable uniform field. This also ensures that the system does not become numerically unstable when the other components drive the system to become periodic. Second is an excess energy ΔF_{ex} that drives the system to a nonuniform periodic structure and is typically responsible for anisotropy in the system as well as for creating topological defects such as dislocations and interfaces. The third component that can enter into the PFC model is a source of energy ΔF_{ext} due to an external source potential. The total free-energy difference ΔF relative to a uniform reference state with density ρ_0 is written as

$$\frac{\Delta F}{\rho_0 k_B T} = \Delta F_{\text{id}} + \Delta F_{\text{ex}} + \Delta F_{\text{ext}}. \qquad (3)$$

This work will focus only on the first two of these energies and their interaction.

A. Local free-energy functional ΔF_{id}

In the CDFT formalism, the local free energy arises from an entropically driven ideal gas or fluid. The ideal component of the PFC free energy can be treated as an expansion of this energy about a reference state or, alternatively, as a polynomial fit to a local free energy,

$$\Delta F_{\text{id}} = \int \{[1 + n(\vec{r})]\ln[1 + n(\vec{r})] - n(\vec{r})\}d\vec{r}$$

$$\approx \int \left[\frac{n(\vec{r})^2}{2} - \nu\frac{n(\vec{r})^3}{6} + \xi\frac{n(\vec{r})^4}{12} \right] d\vec{r}, \qquad (4)$$

where $n(\vec{r}) = \rho(\vec{r})/\rho_o - 1$ is the dimensionless probability density of atomic occupancy normalized to the reference density, and ν and ξ are parameters that correspond to an expansion about a particular reference density. These parameters are treated as adjustable in various models in the literature to help stabilize particular systems of interest.

The first variant of the PFC model used the parameters $\nu = 0$ and $\xi = 3$ in Eq. (4), which results in the lowest order of entropic energy that produces a liquid state in the absence of excess energy $[O(n^2)]$ and that caps the amplitude of emergent
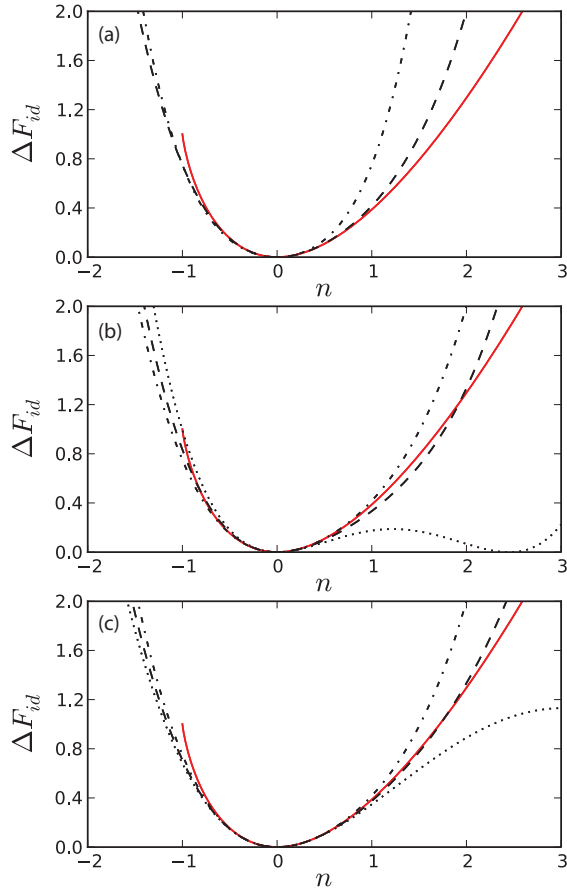
FIG. 1. (Color online) Plots of ΔF_{id}, where in all plots the ideal-gas energy is plotted with a solid line, and the expansion point for the polynomial form of the free energy is $n(\vec{r}) = 0$. Equation (4) with (a) $\nu = 0$ and $\xi = 3$ (dash-dot) and $\nu = 1$ and $\xi = 1$ (dash); (b) $\xi = 1$ and $\nu = 1$ (dash-dot), $\nu = 1.5$ (dash), and $\nu = 2.45$ (dot); and (c) $\nu = 1$ and $\xi = 1$ (dash-dot), $\xi = 0.5$ (dash), and $\xi = 0.1675$ (dot).

periodic structures [$O(n^4)$] in the presence of an excess energy of $O(n^2)$ [21–24,28,36–38]. This produces an *ideal* component to the free energy that is symmetric about the reference density, as illustrated in Fig. 1(a). This symmetry limits the emergence of more complicated periodic structures.

In subsequent extensions of the PFC model, cubic terms in the expansion of the ideal energy were retained (i.e., $\nu = 1$ and $\xi = 1$ in [26]). The addition of this cubic term breaks the symmetry of the energy well around the reference density ($\bar{n} = 0$) and aids in the stabilization of density fields which contain multiple modes. This expansion is formally only valid for density fields that have small amplitudes, but the emergent structures in the model may exhibit large amplitude variations. The parameters ν and ξ have been varied phenomenologically to further stabilize particular phases of interest. Deviations from $\nu = 1$ and $\xi = 1$ can be physically argued to be either expansions about a different reference state, a better polynomial fit to the entropic energy of the material, or to incorporate the lowest-order component of higher-order particle correlation functions [27,39–41]. Tuning ν [see Fig. 1(b)] and ξ [see Fig. 1(c)] leads to better (or worse) approximations of the ideal-gas energy as a function of the local density and can also

be used to aid in mapping to particular physical parameters [20,42]. When constructing ΔF_{ex} in the next section, it will be seen how the symmetry breaking of the free energy around the reference density due to these terms is also crucial in stabilizing certain lattices modes. All of our simulations and energy calculations in later sections use $\nu = \xi = 1$.

B. Excess energy ΔF_{ex}

The nonlocal excess free energy can be constructed to create an energy minimum for a desired periodic structure. This energy has to be properly balanced with the local entropic component of the free energy to produce stable minima of the total free energy for a desired crystal symmetry. The amplitude of the periodic density peaks must also be capped as much as possible to maintain the numerical advantage of the PFC methodology. We will show here how the excess energy can be constructed to stabilize triangular and square lattices in 2D, and bcc, fcc, hcp, and sc lattices in 3D.

In the expansion of the total free energy, the lowest order of particle interactions can be included by an excess energy term that incorporates simple two-particle correlations. This *direct correlation* function ignores local contributions to the free-energy density and assumes only inter-particle interactions, temporally averaged over all particles. This interaction is represented by a convolution of the density field with the direct correlation function $C_2(|r - r'|)$ computed at a mean reference density state ρ_o,

$$\Delta F_{\text{ex}} = -\frac{1}{2} \int n(\vec{r}) \int C_2(|\vec{r} - \vec{r}'|) n(\vec{r}') \, d\vec{r}' \, d\vec{r}. \quad (5)$$

Real space convolutions are conveniently multiplicative in Fourier space, and as such our kernels will be constructed in a Fourier space representation at the mean reference density corresponding to the bulk solid state. To understand how to select $\hat{C}_2(|\vec{k}|)$ in such a way that the free energy has a minima corresponding to a specific lattice, we will first show how the density field behaves due to changes in crystallography.

1. Density field and the reciprocal lattice

At any finite temperature, atoms in a perfect crystal vibrate about their lattice positions. If we assume that the probability of atomic occupancy about any lattice site can be represented by a Gaussian probability distribution, then the entire probability field of the crystal can be represented as a sum over all lattice sites. For example, a 1D lattice representation would be

$$\rho(r) = \sum_i \rho_i(r) = \sum_i \frac{1}{\sigma_v \sqrt{2\pi}} e^{-\frac{1}{2\sigma_v^2}(r - r_i)^2}, \quad (6)$$

where σ_v is the Gaussian width, representing the vibrational amplitude of atoms due to temperature, and r_i is the mean position of lattice point i. The Fourier space representation of the Gaussian lattice site probability has an analytic form

$$\hat{\rho}_i(k) \approx \cos(kr_i) e^{-\frac{1}{2}\sigma_v^2 k^2}. \quad (7)$$

The two components of this transform are quite instructive to understand the stabilization of structures in the PFC formulation. When summed over lattice sites, the components $\cos(kr_i)$ interfere to produce successive δ-peaks corresponding
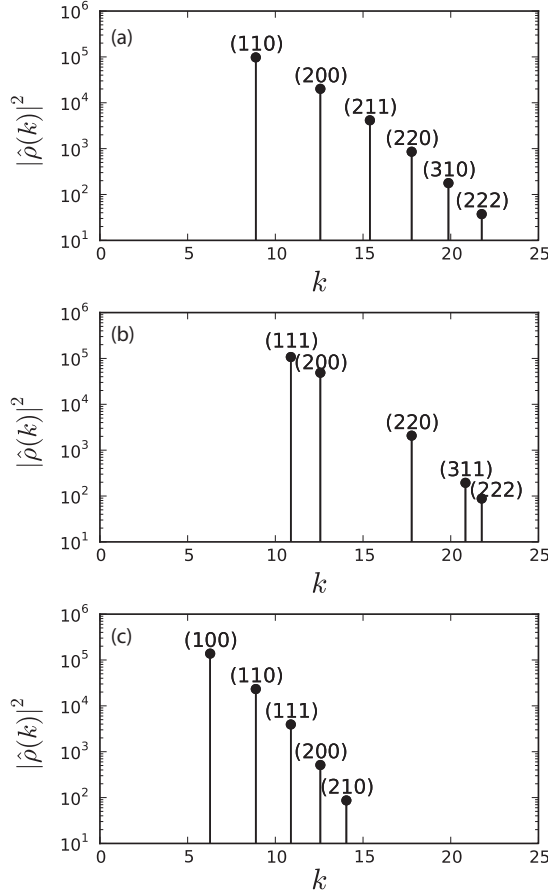
FIG. 2. Fourier space representation of 3D lattices, where the wave vector k is given in units of the inverse lattice spacing $a = 1$. Spectral peaks for (a) bcc, (b) fcc, and (c) sc lattices are plotted for $\sigma_v = 0.05$.

to periodic planes. For an infinite lattice, families of peaks emerge, each corresponding to a set of planes. Each family's peaks occur at integer multiples of that family's fundamental planar frequeny. Figure 2 shows examples of such peaks for bcc, fcc, and sc lattices. The factor $e^{-\frac{1}{2}\sigma_v^2 k^2}$ causes these peaks to decay at a rate corresponding to the Gaussian width and is known as the Debye-Waller coefficient. For high temperatures (large σ_v) close to melting, this term cuts off the higher modes in each family. A modification of this peak structure is used below to construct an effective correlation kernel for the excess free energy. Successively higher frequency modes can be used to progressively reduce the excess energy and stabilize a crystal structure. However, the tradeoff for this additional small stabilization is a large decrease in grid spacing to resolve the resultant sharp density peaks. Therefore, we will include only the first and most dominant peak corresponding to each family. For example, for the Fourier space representation in Fig. 2(a), there are two peaks for the {110} family of planes. Only the first of these two peaks will be considered.

2. Correlation function peak selection

The question of which peaks to represent in the excess free-energy kernel can be answered from an analysis of the energy contribution of each density peak to the total excess

energy. To illustrate this, the energy contributions from the first two peaks of an fcc phase are calculated explicitly and compared to the corresponding energies from a two-peak bcc energy kernel. Consider an approximation to the density field for an fcc lattice that contains modes corresponding to the (111) and (200) planes, the two most dominant peaks shown in Fig. 2(b). The density field of the fcc lattice is approximated by

$$n(x,y,z) = n_{111} + n_{200},$$

$$n_{111} = A_{111} \sum_{h,k,l=\pm 1} \cos[k_o(hx + ky + lz)], \qquad (8)$$

$$n_{200} = A_{200}\{\cos(2k_o\,x) + \cos(2k_o\,y) + \cos(2k_o\,z)\},$$

where $k_o = 2\pi$ sets the fcc lattice parameter $a = 1$, h,k,l are the Miller indices, and A_{111} and A_{200} are amplitudes to be solved for by energy minimization.

In this approximation, the total excess energy in Eq. (5) can be broken down into four contributing parts by substituting Eq. (8). We neglect the cross density terms since integration over the unit cell results in zero contributions to the energy for these terms, and we are left with independent energy components that depend strictly on n_{111} and n_{200}, respectively. Specifically, the energy per unit volume becomes

$$\frac{\Delta F_{\text{ex}}}{V} = -\frac{1}{2a^3} \int n_{111}(\vec{r}) \int C_2(|\vec{r} - \vec{r}'|) n_{111}(\vec{r}')\, d\vec{r}'\, d\vec{r}$$

$$-\frac{1}{2a^3} \int n_{200}(\vec{r}) \int C_2(|\vec{r} - \vec{r}'|) n_{200}(\vec{r}')\, d\vec{r}'\, d\vec{r}. \quad (9)$$

First we consider the contribution from the dominant plane for the fcc lattice, the (111) plane illustrated in Fig. 2(b). The convolution is calculated using the Fourier transform of $C_2(|\vec{r} - \vec{r}'|)$, denoted $\hat{C}_2(|\vec{k}|)$, and the Fourier transform of $n(x,y,z)$, denoted $\hat{n}(\vec{k})$. The correlation function contributes a constant multiplier to the total free energy for each mode in a perfect lattice and is factored out of the sum. Since the cross terms over the Miller indices integrate out to zero over the unit cell, the resulting free-energy change per unit volume integrates to

$$\frac{\Delta F_{\text{ex}(111)}}{V} = -\frac{1}{2a^3}\beta_{111}A_{111}^2\hat{C}_2(k_1), \qquad (10)$$

where $k_1 = \sqrt{3}k_o$ and $\beta_{111} = 8$ is the degree of symmetry of that plane about a reference lattice position. Repeating this procedure for the (200) plane leads to an energy of

$$\frac{\Delta F_{\text{ex}(200)}}{V} = -\frac{1}{2a^3}\beta_{200}A_{200}^2\hat{C}_2(k_2), \qquad (11)$$

where $k_2 = 2k_o$ and $\beta_{200} = 6$ due to lattice symmetry.

Repeating the above process for a bcc lattice and with correlation peak maxima corresponding to the bcc density modes leads to energies of

$$\frac{\Delta F_{\text{ex}(110)}}{V} = -\frac{1}{2a^3}\beta_{110}A_{110}^2\hat{C}_2(k_1),$$

$$\frac{\Delta F_{\text{ex}(200)}}{V} = -\frac{1}{2a^3}\beta_{200}A_{200}^2\hat{C}_2(k_2), \qquad (12)$$

where $k_1 = \sqrt{2}k_o$, $k_2 = 2k_o$, $\beta_{110} = 12$, and $\beta_{200} = 6$.

We next minimize the sum of ideal and excess free energies, assuming correlation kernels satisfying $\hat{C}_2(k_1) = \hat{C}_2(k_2) = 1$

for the modes of both bcc and fcc phases (i.e., the particles are completely correlated). This leads to the amplitudes $A_{110} = 0.13237$ and $A_{200} = 0.05573$ for bcc and $A_{111} = 0.14274$ and $A_{200} = 0.10648$ for fcc. These numbers yield relative energy contributions $\Delta F_{111}/(\Delta F_{111} + \Delta F_{200}) = 0.706$ for fcc and $\Delta F_{110}/(\Delta F_{110} + \Delta F_{200}) = 0.919$ for bcc. The fcc and bcc correlation functions can be compared by substituting these amplitudes into the energy [Eqs. (10)–(12)]. In the present approximation, about 92% of the bcc excess energy is stored in the first correlation peak, while the excess free energy of the fcc structure is split about 70%–30% between its first two correlation peaks.

Stabilization of the sc phase requires three peaks in the correlation kernel. These peaks correspond to the (100), (110) and the (111) planes. The first two density peaks in Fig. 2(c) for the sc kernel are shared with a bcc kernel, with a different lattice spacing. In the bcc phase, 98% of the free energy is stored in these two peaks. The addition of the third peak stabilizes the sc lattice, but the energy difference between the two phases is only about 2%. The sc structure (and other higher mode structures) can be further stabilized by making the well of the local free-energy density (Fig. 1) more asymmetric about the reference density. This, however, leads to sharper density peaks and requires more computer memory to store finer numerical meshes.

The above analysis reveals several important points. The first, and most important, point in constructing a correlation function that stabilizes the fcc structure is to realize that inclusion of only a single peak in the correlation function will always stabilize the bcc structure at the solid reference density ρ_o (i.e., $\bar{n} = 0$). Therefore, the second peak must be included to stabilize the fcc structure [16]. It turns out that including a third peak in the excess energies leads to relative changes in the energy of less than 1% for both of these phases, and as such these peaks can be omitted. A further revelation in this construction comes in a study of the emergent anisotropy of the crystalline phases. This is discussed below in Sec. IV.

3. Direct correlation function construction

The previous section showed how the density field's spectral peaks emerge and how they contribute to the free energy. In this section, the form of the excess free-energy kernel $\hat{C}_2(|\vec{k}|)$ is constructed to include relevant reciprocal space peaks at positions determined by the desired crystal unit cell. The positions of the peaks correspond to the interplanar spacings shown by the δ-peaks in Fig. 2. The peaks of our $\hat{C}_2(|\vec{k}|)$ have a finite width, discussed further below. The excess free energy also contains a temperature parameter, crucial for driving phase transformations.

For the fcc, bcc, and hcp kernels we select two modes, each corresponding to the two most dominant peaks in the density spectrum. The resulting functions $\hat{C}_2(|\vec{k}|)$ are illustrated in Fig. 3(a) for the case of zero temperature ($\sigma = 0$). The lattice spacings of all three structures are scaled such that the lowest frequency peaks of all correlation functions overlap to illustrate the relative positions of the secondary peaks. Individual peaks are represented in reciprocal space by Gaussians of the form $\exp[-\frac{(k-k_i)^2}{2\alpha_i^2}]$, with a finite width of α_i rather than the δ-peaks of a perfect lattice. The variation of the parameter α_i accounts
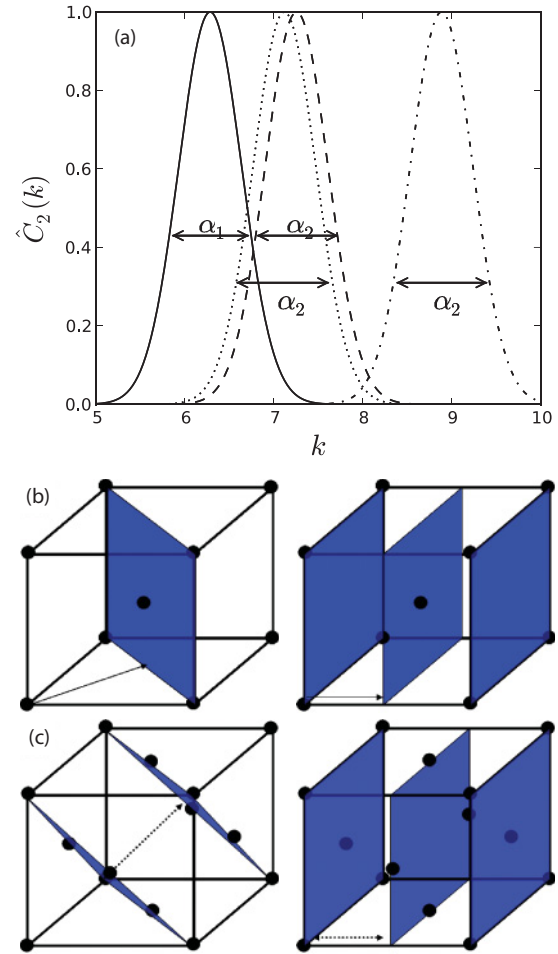
FIG. 3. (Color online) (a) Two peak correlation functions $\hat{C}_2(k)$ for hcp (dot), fcc (dash), and bcc (dash-dot) lattices. In this illustration, the lattice spacing has been rescaled such that the first peak of the function overlaps for all three lattices. For simplicity, the case of zero effective temperature is shown here (i.e., $\sigma = 0$). α_1 and α_2 are free parameters that set the width of each peak correspondingly. Planes illustrating the planar symmetry and the planar atomic density are shown in (b) for bcc (110) (dominant) and (200) planes and (c) for fcc (111) (dominant) and (200) planes.

for changes in the free energy due to interfaces, defects, and strain. Specifically, varying α_i changes the width of a liquid-solid interface, which directly affects the surface energy [35, 43] and can control the magnitude of the elastic coefficients and their anisotropy.

The effect of temperature enters into our correlation function via modulation of the Gaussian peak heights. This modulation is motivated by the Debye-Waller decay due to thermal motion of atoms about their equilibrium positions. A prefactor to this effect is also included that accounts for the number of planar symmetries β_i (dimensionless) and for the atomic density ρ_i within each plane. For instance, the bcc (200) plane has an atomic density of $\rho_{200} = 1$ and a planar symmetry of $\beta_{200} = 6$, which can be inferred from Fig. 3(b). These factors represent the relative weight of each planar family and give each its own corresponding Debye-Waller prefactor. These effects are accounted for phenomenologically by modulating the peaks in $\hat{C}_2(k)$ by the factor $\exp[-(\sigma^2 k_i^2)/(2\rho_i\beta_i)]$, where

σ plays the role of an effective temperature. Summarizing, each *family* of planes i in the unit cell thus contributes a peak to the correlation kernel of the form

$$\hat{C}_2(k)_i = e^{-\frac{\sigma^2 k_i^2}{2\rho_i \beta_i}} e^{-\frac{(k-k_i)^2}{2\alpha_i^2}}. \tag{13}$$

The complete correlation function in Fourier space [i.e. Fig. 3(a)] comprises the numerically evaluated *envelope* of the superposition of all relevant peaks for the crystal structure given by Eq. (13). This avoids shifts in the peak positions and, correspondingly, changes to the stable structure that would result from a simple sum of these peaks. It is noted that this technique leads to stable structures that exist around the *reference* state of the energy. Through the use of α_1 and α_2, which modulate the correlation function peaks, the anisotropic response of a given crystal structure can be tuned, as discussed later in Sec. IV.

III. EQUILIBRIUM PROPERTIES

This section examines some of the equilibrium properties of the PFC materials that emerge from the formalism discussed above. First we construct the phase diagram corresponding to the fcc correlation function using a numerical method for minimizing the energy. The effect of the $k = 0$ mode on the periodic structure is examined separately by using a square correlation function. Finally, we demonstrate the robustness of our methodology to generate even more complex structures by showing an example of dynamic coexistence of an hcp seed growing into a liquid melt, using an energy kernel for an hcp lattice.

A. Phase diagram construction

Phase coexistence is analyzed by performing a common tangent construction between the curves of free energy versus average density of different combinations of bulk phases. The free energy of a phase is calculated at each average density by iterative relaxation of the total free-energy functional, using the kernel for the structure of interest, as described in Sec. II B. A phase diagram for a liquid-bcc-fcc system using a correlation kernel for a fcc lattice is shown in Fig. 4(a). The free-energy curves shown in Fig. 4(b) are computed for liquid, bcc, and fcc states by varying the mean density, and for each mean density imposing the corresponding density structure, and numerically minimizing the amplitudes of the density peaks.

The liquid state energy is computed assuming a constant density for all values of $\bar{n}$, and the energy per unit volume is calculated by numerically integrating Eq. (3). The bcc and fcc crystal structures are initially set up by imposing a series of Gaussian density peaks at lattice positions in a numerical domain with lattice spacings of $a = 1$ for the fcc phase and $a = \sqrt{2/3}$ for the bcc phase. These density fields are numerically relaxed by iterating Eq. (2) in Fourier space. The relaxed energy density is integrated over the crystal unit cell, yielding free energy versus mean density $\bar{n}$ for an effective temperature σ. Varying the effective temperature σ thus produces the phase diagram shown in Fig. 4(a). It is noteworthy that a stripe phase is not stable in our model. The reason for this is related to the lack of cross terms of modes in the expansion of the density field, i.e., the
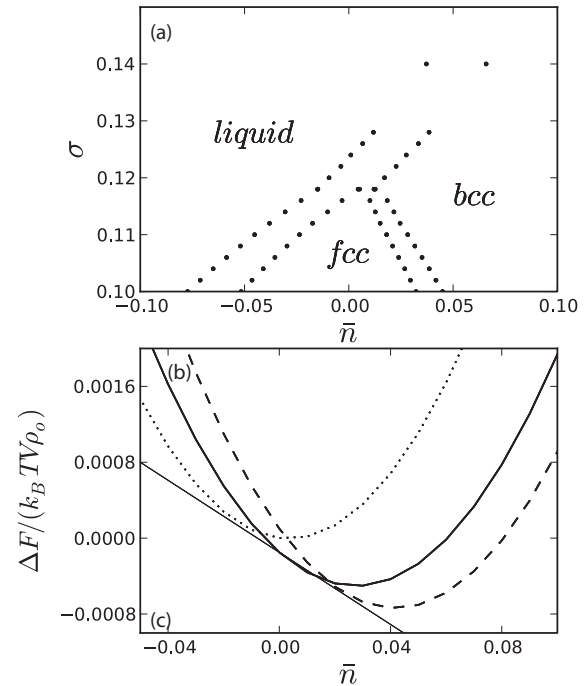
FIG. 4. (a) Phase diagram for an fcc lattice correlation function showing the coexistence between liquid, fcc, and bcc phases near a peritectic point. (b) Free-energy curves for the liquid (dot), fcc (solid), and bcc (dash) phases at a temperature close to the peritectic point of the phase diagram.

$n(\vec{r})^3$ term in the free energy integrates to zero for this crystal symmetry.

As the temperature is increased, the lower-frequency modes of the correlation function become dominant in the free energy over the higher-frequency modes, which changes the particular structure that minimizes the free energy. For example, as σ increases, the fcc crystal transforms into a bcc crystal since the bcc structure minimizes the free energy when only a single mode is present in the correlation kernel. This is consistent with the free-energy ratios examined in Sec. II, where it was seen that 92% of the bcc energy is due to the first correlation peak. The decay of peaks leads to a transformation of coexisting liquid and solid phases into a single solid phase at a peritectic point.

B. Effect of the $k = 0$ mode

The $k = 0$ mode in the correlation function affects the bulk compressibility of a material. For simplicity, the $k = 0$ value of the correlation function in Fig. 3 is set to zero. It must be stressed, however, that the introduction of a nonzero $k = 0$ contribution to the correlation kernel does not affect the stability of the various structures discussed above. Its effect is instead to compress the phase diagram about the reference density ($\bar{n} = 0$) around which the free-energy functional is expanded. We illustrate this effect by examination of the free-energy curves for two different phases.
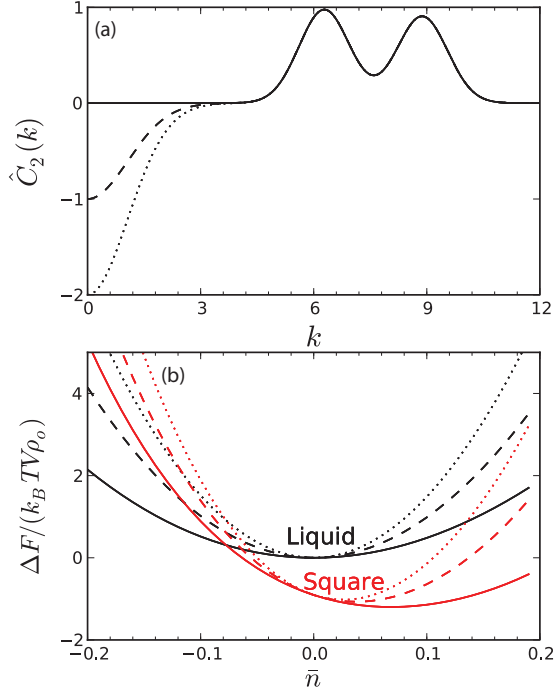
FIG. 5. (Color online) Effect of the $k = 0$ mode illustrated using the 2D square correlation function. (a) Correlation functions with different $k = 0$ mode amplitudes: $\hat{C}_2(0) = 0$ (solid), $\hat{C}_2(0) = -1$ (dashed), and $\hat{C}_2(0) = -2$ (dotted). (b) Effect of the $k = 0$ mode on the phase stability illustrated by free-energy curves for the liquid (black) and square (red/gray) phases for the three amplitudes shown in (a).

We will consider here a liquid and a square lattice in 2D using an energy kernel for a square lattice.[1] As described in Sec. II, we construct our direct correlation function by introducing two peaks corresponding to the modes of the square lattice. However, we now include a third Gaussian peak (with negative amplitude) at $k = 0$ as shown in Fig. 5(a) for an effective temperature of $\sigma = 0.05$. Changing the amplitude of the $k = 0$ mode results in a shift in the free energy for the structures at densities away from the reference density. In our PFC model, the lowest free-energy structure of the correlation kernel is constructed to be stable at $\bar{n} = 0$. This is illustrated in Fig. 5(b) for free-energy curves of both the liquid and square phases. As the mean density of the system is varied away from the reference state density, the change in free energy is steeper for more negative amplitudes of $\hat{C}_2(0)$, that is, the bulk modulus is larger. In all cases the relative energy at the reference state is unchanged, as one would expect since our reference energy state is taken to correspond to a density with a correlation kernel with zero amplitude at $k = 0$.

Previous PFC models have been reported to support stable fcc and hcp structures, but only at very deep quenches where the asymmetry of the ideal energy approximation brings the free-energy state of these lattices to be comparable to the bcc structure at mean densities away from the reference density

---

[1]The liquid-square-triangle phase diagram is published in [35] without a $k = 0$ mode. We note that the σ axis of the phase diagram in [35] is incorrectly labeled and should actually be divided by 2π.

[30,31]. However, by making the $k = 0$ mode of the correlation function deeper, these structures will become unstable due to the liquid phase becoming more preferable at densities away from $\bar{n} = 0$. This stability away from the reference state will also lead to an undesired increase in the density amplitudes as the strength of the $k = 0$ mode of the correlation function is increased. This is not the case for models such as the present one, where the structure of interest is stable at the reference state.

C. Dynamic coexistence

Extending the above methodology to other simple crystalline phases such as hcp and sc lattices is straightforward. Using the secondary peak in the kernel corresponding to the hcp lattice in Fig. 3(a), the hcp structure becomes the stable structure for a range of effective temperatures and densities, as illustrated by the energy curves shown in Fig. 6(b). An hcp lattice with spacings of $a = 1$ and $c = 2\sqrt{2/3}$ emerges using a correlation function with these two primary peaks corresponding to planes with modes of $k_1 = 2\pi\sqrt{4/3}$ and $k_2 = 2\pi\sqrt{41/24}$. The hcp phase can be shown to have dynamic coexistence with the liquid phase by seeding the liquid phase with an hcp nucleus that has a sufficient radius to overcome surface energy melting. We set the material parameters to values of $\alpha_1 = \alpha_2 = 1.0$ allowing a small nucleation radius to survive due to low surface energy. The temperature is quenched to a value of $\sigma = 0.02$ and, corresponding to the
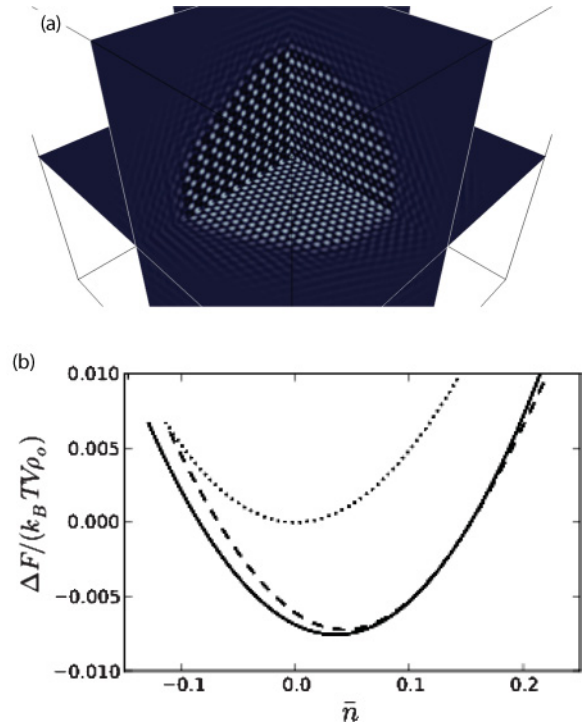
FIG. 6. (Color online) (a) Dynamic coexistence of hcp with a liquid. Three perpendicular planar cuts through the simulation volume are shown illustrating the hcp structure. (b) Free-energy curves for a quench using an hcp correlation function shown for the liquid (dot), bcc (dash), and hcp (solid). The energies clearly show the stability of the hcp lattice relative to a minimized bcc and liquid state at the reference density ($\bar{n} = 0$).

energy curves of Fig. 6(b), we set the hcp lattice density initially to a value of $\bar{n}_{hcp} = 0.0$ and the total mean density of the system to $\bar{n} = -0.09$. The system is evolved using the dynamics of Eq. (2). The hcp seed grows, at first linearly in velocity, slows, and eventually reaches coexistence with the liquid phase. This coexistence is illustrated in Fig. 6(a), showing three perpendicular cuts through the system volume. These cuts clearly show the stable a-b-a-b stacking of hcp and the triangular arrangement of the (0001) plane. Both fcc and sc phases also coexist dynamically with the liquid phases using their appropriate energy kernels.

IV. ELASTICITY

This section computes cubic elastic moduli C_{11}, C_{12}, and C_{44} for the 2D square and 3D fcc free-energy functionals at their respective reference densities. We extract the moduli by Taylor expansion of the energy about specific strained states of the defect-free lattices. For the square lattice, we calculate the strain energy both numerically and analytically through a two-mode approximation and find excellent agreement between the two methods. Since the numerical approach is too costly for small strains in 3D, the equivalent calculation for the fcc lattice is performed only analytically.

A. 2D square phase elastic coefficients

The elastic coefficients are computed by fitting free energy curves to specific strain states. For a square lattice using a square energy functional, it is necessary to consider three strain states: bulk, deviatoric, and simple shear. The free energy of these strained states can be expanded as

$$\begin{aligned} \Delta F_{\text{bulk}} &\approx F_o + m_b \delta^2 + O(\delta^4), \\ \Delta F_{\text{dev}} &\approx F_o + m_d \delta^2 + O(\delta^4), \\ \Delta F_{\text{shear}} &\approx F_o + m_s \delta^2 + O(\delta^4), \end{aligned} \quad (14)$$

where F_o is the unstrained energy state and δ is the magnitude of the strain. The bulk, deviatoric, and shear strain states are defined here as $n(x/(1 + \delta), y/(1 + \delta))$, $n(x(1 + \delta), y(1 - \delta))$, and $n(x + \delta y, y)$, respectively. In 2D, m_b, m_d, and m_s are quadratic fit parameters related to the elastic coefficients by $m_b = C_{11} + C_{12}$, $m_d = C_{11} - C_{12}$, and $m_s = C_{44}/2$ [22]. Two methods of computing the energy curves for the bulk, deviatoric, and simple shear strains are implemented. We consider the case in which $\alpha_1 = \alpha_2$ in the correlation function.

1. Numerical calculation of elastic coefficients

The first approach we consider is to numerically strain a relaxed periodic density field. To accomplish this, we use a domain size fitting 40 unit cells in each dimension with an initial mesh spacing of $dx = 0.05$ corresponding to a lattice spacing of $a = 1$ in dimensionless units. The simulation domain is filled with overlapping Gaussian density peaks $n_i = \exp\{-[(x - x_i)^2 + (y - y_i)^2]/(2\sigma_v^2)\}$, where i is summed over all lattice sites for a square lattice. With the Gaussian representation of the field in place, the mean density field is shifted to the reference density ($\bar{n} = 0$) and then relaxed to its minimum energy state using the dissipative dynamics of Eq. (2). This yields the unstrained base energy F_0.

The bulk strain can by applied to our base state by varying the mesh spacing as $dx' = dx/(1 + \delta)$. With this *strained* state of the lattice, the energy per unit cell is integrated numerically and fitted to Eq. (14), where the coefficient m_b is easily extracted. Results for m_b are shown for the case of $\sigma = 0$ as open circles in Fig. 7(a) for various values of $\alpha_1 = \alpha_2$. Simple shear and deviatoric strains are similarly computed by mesh manipulation of our base state. The mesh is sheared by the coordinate transform on the grid points N by $N(x(1 + \delta), y(1 - \delta))$ and $N(x + \delta y, y)$. To calculate the energy via Fourier transform techniques, the sheared mesh is mapped back onto a uniform mesh by linear interpolation. The periodic nature of the system yields good results for simple shear, but deviatoric strains result in accurate values for the energy only when the applied strain resulted in multiple values of the lattice spacing in both x and y (i.e., the lattice periodicity fits in the system). For small strains, our calculations therefore require very large system sizes to accurately compute the energy values. As a result, this technique is not practical in 3D.

2. Analytical calculation via a two-mode approximation

A second approach to calculate strained free energies employs a two-mode approximation to the density field. To lowest order, the density requires two amplitudes to have enough freedom to minimize with regard to our two-peak correlation function. The density field of a square lattice can be written as

$$\begin{aligned} n(x, y) &= A_{10}[(3\sqrt{2} - 2)\cos(k_o y) - 2\cos(k_o x)] \\ &\quad - A_{11}\cos(k_o x)\cos(k_o y), \end{aligned} \quad (15)$$

where A_{10} and A_{11} are amplitudes to be solved for by energy minimization. The limitation of this approach is that since our correlation function is the envelope of overlapping peaks, it is not possible generally to obtain a closed-form mathematical expression for the elastic coefficient. However, in the limit of small α_i, when the peaks do not overlap, our correlation function can be described analytically as

$$C_2(|\vec{k}|) = \sum_i e^{-\frac{1}{2\alpha_i^2}(|\vec{k}| - k_i)^2}, \quad (16)$$

where i indexes over the correlation function peaks.

With these approximations, we can calculate our base state energy by minimizing the energy for an unstrained square lattice. The amplitudes A_{10} and A_{11} are calculated taking the Fourier transform of Eqs. (15) and (16) to compute the convolution in the excess free energy $\hat{K}(k_x, k_y) = \hat{C}_2(|\vec{k}|)\hat{n}(k_x, k_y)$. The energy per unit volume can now be calculated from

$$\frac{\Delta F}{V} = \frac{1}{a^2} \int_0^a \int_0^a dx\, dy \left[\Delta F_{\text{id}} - \frac{n(x, y)}{2} K(x, y) \right], \quad (17)$$

where $\nu = \xi = 1$ gives a function dependent on A_{10} and A_{11}. This free energy is minimized by solving the system of equations $\partial \Delta F/\partial A_{10} = 0$ and $\partial \Delta F/\partial A_{11} = 0$. For a lattice spacing of $a = 1$ and a temperature of $\sigma = 0$, the amplitudes are found to be $A_{10} = 0.218\,24$ and $A_{11} = 0.560\,15$. The resultant density structure for an unstrained crystal was found to be in very good agreement with the numerically minimized structure, as shown in Fig. 7(a).

The energy for the bulk, deviatoric, and shear strained lattices is calculated by substitution of their respective coordinate transformations into the density field [Eq. (15)]. The strained energy is extracted by repeating the energy integration above, except now the bounds of integration are over the strained unit cell. We assume (confirmed but not shown here) that for small strains, the amplitudes A_{10} and A_{11} have negligible changes for the regime we study. These energy curves are fit to the parabolic order of Eq. (14) to extract the coefficients m_b, m_d, and m_s.

3. Comparison of the elastic coefficients

Figure 7(a) compares the analytically evaluated coefficient m_b (filled circles) to their numerically determined counterparts for the same values of α_i. Both solutions agree very well until the correlation peak widths overlap. This is due to a shift in the peak's position by the sum in Eq. (16) causing a deviation from the correlation function used numerically. This deviation
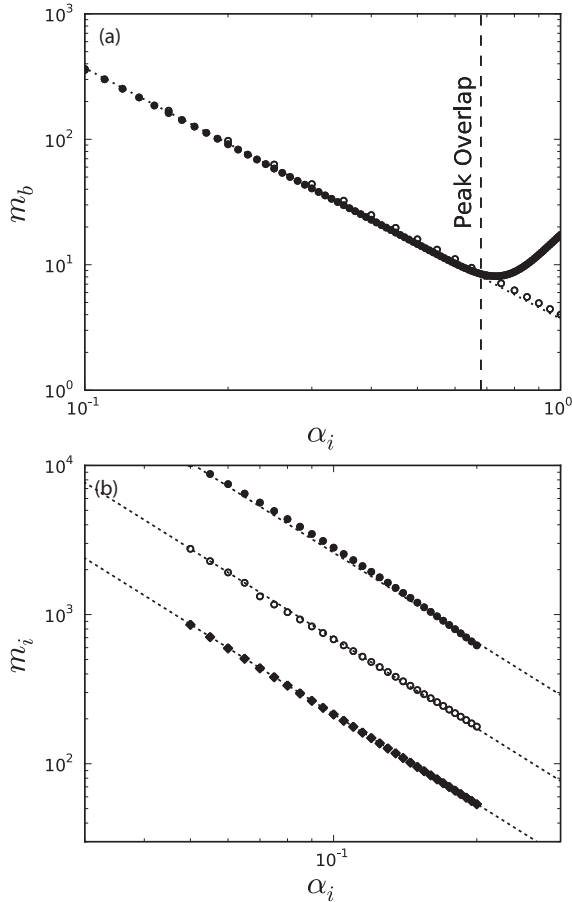
FIG. 7. (a) Elastic coefficient $m_b = (C_{11} + C_{12})$ for a square lattice from Eq. (14) as a function of correlation peak widths $\alpha_1 = \alpha_2$. Numerical (open circles) and analytical (filled circles) results are shown and fitted to Eq. (18) (dot). (b) Elastic coefficients m_b, m_o, and m_s for the fcc lattice for bulk (filled circle), orthorhombic (open circle), and simple shear strain (filled diamonds) states as a function of the correlation function peak widths $\alpha_1 = \alpha_2$. Dotted lines shows fits to Eq. (18).

is marked in Fig. 7(a) by "Peak Overlap." Similar agreement is found for the other coefficients m_d and m_s. All coefficients follow a power-law function over all tested α_i values,

$$m_j = A_j \alpha_i^{-2}, \tag{18}$$

where A_j represents a fitting coefficient for the different shear states. These values are $A_b = 3.7$, $A_d = 2.1$, and $A_s = 0.35$ for the bulk, deviatoric, and shear states when $\alpha_1 = \alpha_2$.

B. 3D fcc phase elastic coefficients

The elastic coefficients for the fcc phase are computed using the analytic method described above. For cubic lattices, it is necessary to consider three strain states: bulk, orthorhombic, and simple shear [44–47]. These constituent strains are also fitted to quadratic order in an expansion of the free energy,

$$\begin{aligned}
\Delta F_{\text{bulk}} &\approx F_o + m_b \delta^2 + O(\delta^4), \\
\Delta F_{\text{orthorhombic}} &\approx F_o + m_o \delta^2 + O(\delta^4), \\
\Delta F_{\text{shear}} &\approx F_o + m_s \delta^2 + O(\delta^4).
\end{aligned} \tag{19}$$

The bulk modulus is related to the curvature of the free energy and can be described as

$$B(V) = V \frac{\partial^2 \Delta F}{\partial V^2}, \tag{20}$$

where V is the deformed volume of the unit cell. The volumetric strain on the lattice is described by the strain tensor

$$\epsilon_{\text{bulk}} = \begin{vmatrix} \delta & 0 & 0 \\ 0 & \delta & 0 \\ 0 & 0 & \delta \end{vmatrix}, \tag{21}$$

and therefore $V = a^3(1 + \delta)^3$. The relationship between m_b and the bulk modulus is obtained by substituting the energy expansion of Eq. (19) into the bulk modulus Eq. (20), solving for m_b, and expanding, $m_b = \frac{9}{2}B + O(\delta)$. By dropping the higher-order terms in m_b, we neglect volumetric changes to the bulk modulus. The elastic coefficients can be obtained from the bulk modulus $B = (C_{11} + 2C_{12})/3$ in conjunction with the other constituent strains.

To solve for the elastic coefficients, we also need to use two volume-conserving (to linear order in δ) strain states. First is an orthorhombic shearing of the lattice described by the strain tensor,

$$\epsilon_{\text{orthorhombic}} = \begin{vmatrix} \delta & 0 & 0 \\ 0 & -\delta & 0 \\ 0 & 0 & \delta^2/(1 - \delta^2) \end{vmatrix} \tag{22}$$

and second is a simple shear defined by the strain tensor,

$$\epsilon_{\text{shear}} = \begin{vmatrix} 0 & \delta/2 & 0 \\ \delta/2 & 0 & 0 \\ 0 & 0 & \delta^2/(4 - \delta^2) \end{vmatrix}. \tag{23}$$

The final fitting parameter relationships used in Eq. (19) are $m_b = \frac{3}{2}(C_{11} + 2C_{12})$, $m_o = C_{11} - C_{12}$, and $m_s = C_{44}/2$.

The density field of the fcc phase is approximated by the two-mode density field used earlier in Eq. (8). The base state of the unstrained lattice is calculated by integration over the unit cell, and the amplitudes of the fcc phase can be

found in Sec. II B 2. Substitution of A_{111} and A_{200} into the density field approximation results in a minimized energy state for the density structure of an unstrained fcc crystal. The strained state energies are integrated over the now strained unit cells, and these energy curves are fit to the quadratic approximations of Eq. (19). Once again, it was found that the free-energy coefficients m_b, m_o, and m_s follow a power-law function Eq. (18) over all tested α_i values; see Fig. 7(b). The corresponding fit coefficients are $A_b = 26$, $A_o = 6.9$, and $A_s = 2.15$ for the bulk, orthorhombic, and shear states when $\alpha_1 = \alpha_2$.

C. Temperature dependence of elastic coefficients

The effective temperature σ modulates the peak heights in the correlation function, which changes the elastic moduli. The magnitude of the change is additionally dependent on the peak widths α_i. As an example, Fig. 8(a) shows the relative change of m_b for the fcc lattice with temperature for several values of $\alpha_1 = \alpha_2$. The coefficient decreases with increasing temperature; larger values of α_i cause a slower decrease. We find that the temperature behavior can be well described by a quadratic form,

$$m_b = m_b^o - b_\alpha \sigma^2, \tag{24}$$
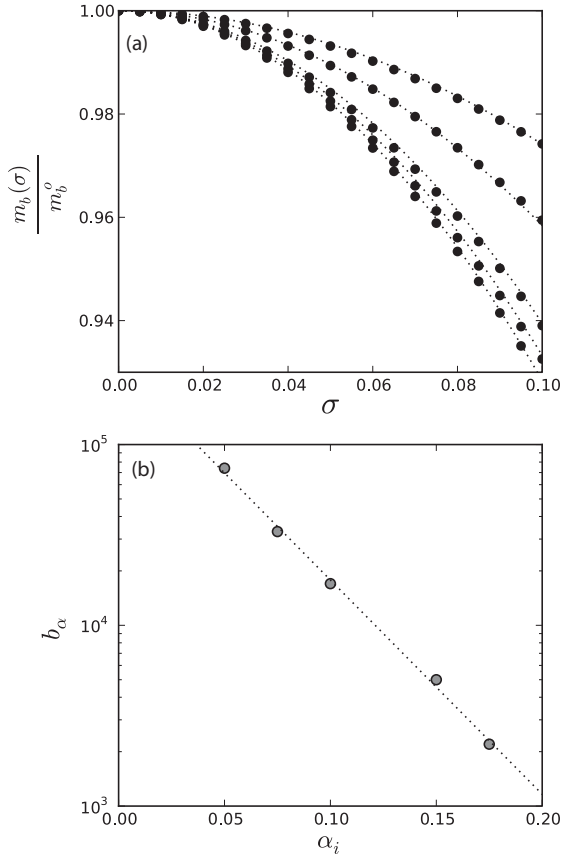
FIG. 8. (a) Relative change in the elastic coefficient m_b with temperature σ for several correlation peak widths $\alpha_1 = \alpha_2 = 0.05$, 0.075, 0.1, 0.15, and 0.175 (bottom to top). (b) Dependence of the quadratic fit coefficient b_α in Eq. (24) on α_i. Dotted line shows an exponential fit (see text).
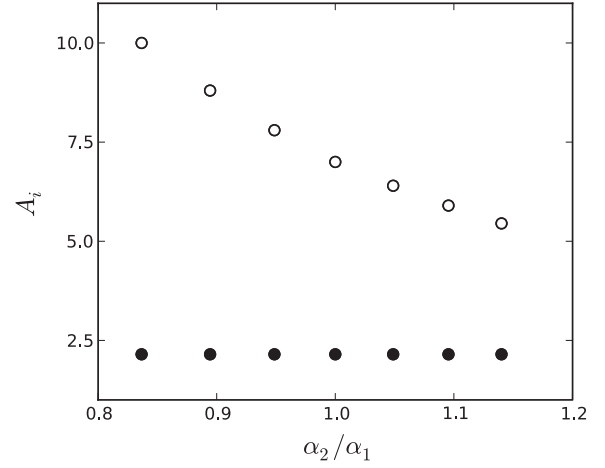
FIG. 9. Elastic coefficient prefactors A_i as a function of α_2/α_1 for the orthorhombic strain A_o (empty circle) and simple shear A_s (filled circle).

where m_b^o is the value of m_b when $\sigma = 0$. The dependence of the fit coefficient b_α on α_i is explored in Fig. 8(b), where it can be well fit to an exponential form $b_\alpha = B_1 e^{-B_2 \alpha_i}$ with $B_1 = 2.74 \times 10^5$ and $B_2 = 27.335$.

D. Tuning anisotropy

The magnitude of the material's elastic anisotropy plays an important role in defect interactions. Here we show how anisotropy enters into the model through a coupling of the density field and its interaction in the energy with the modes included in our correlation kernel. Elastic anisotropy can be characterized by the deviation from the isotropy relation,

$$C_{44} = (C_{11} - C_{12})/2. \tag{25}$$

We repeat the energy calculation in the previous two sections, but now instead of varying the temperature σ or the magnitude of the peak widths $\alpha_1 = \alpha_2$, we investigate the effect of varying the ratio of peak widths α_2/α_1. For these tests, an fcc kernel is used with $\sigma = 0$, and we consider the free energies of the two volume-conserving strain states. Figure 9 illustrates the effect on m_o and m_s as we vary α_2 relative to α_1. The first peak of the correlation function was set to a value of $\alpha_1 = 0.175$ such that the two peaks would not overlap for the range of this calculation. Interestingly, we find that as α_2 is varied, the amplitude of the simple shear component A_s [Eq. (18)] varies very little while the orthorhombic amplitude A_o has a large dependence on the relative size of α_2 and α_1. The condition for elastic isotropy can be determined by substitution of Eq. (18) into Eq. (25), giving a relationship of

$$A_o = 4A_s. \tag{26}$$

This implies that the ratio α_2/α_1 must equal the ratio of the first two peak positions; for an fcc crystal, $\alpha_2/\alpha_1 = \sqrt{3}/2$.

V. DISCUSSION

We have introduced an extension for the phase-field-crystal (PFC) model to self-consistently construct free energy kernels

that produce targeted crystal structures. We explicitly showed that this method produces energetically stable bcc, fcc, hcp, and sc phases for appropriately selected free-energy kernels containing multiple peak two-point correlation functions. For the fcc and hcp phases, it was shown that two peaks are sufficient to stabilize the structures at the reference density, while three peaks are needed to stabilize the sc phase. We also explicitly showed how to map out the elastic coefficients and how to tune the elastic anisotropy by adjusting the peak curvature through changes in the correlation function peak widths.

The resulting dependence of the anisotropy strength on the relationship between peak widths has implications if we consider the relative change between the fcc and the bcc phases. As shown in Sec. II, the energy spread across the two primary peaks for the bcc and fcc lattices in the PFC model is 92%–8% for the bcc phase and about 70%–30% for the fcc phase. This will naturally result in a greater anisotropic response in the fcc lattice since the response is related to the relative changes in energy between these two modes.

The close proximity of the secondary peak of the fcc and hcp phases can also have implications for the relative stability of the two phases. Increasing the width of the second peak for the fcc phase will increase the stability of a metastable hcp phase. As shown in Fig. 9, this increase in width results in an effective decrease in the shear modulus, relative to the total magnitude of the elastic coefficients. This could potentially decrease slip barrier energies, facilitating the use of the PFC model to investigate dislocation splitting, creating hcp planes.

ACKNOWLEDGMENTS

[1] W. Boettinger, J. Warren, C. Beckermann, and A. Karma, Annu. Rev. Mater. Res. **32**, 163 (2002).

[2] L. Chen, Annu. Rev. Mater. Res. **32**, 113 (2002).

[3] N. Provatas, M. Greenwood, B. Athreya, N. Goldenfeld, and J. Dantzig, Int. J. Mod. Phys. B **19**, 4525 (2005).

[4] I. Steinbach, Modell. Simul. Mater. Sci. Eng. **17**, 073001 (2009).

[5] D. Bacon, Y. Osetsky, and D. Rodney, in *Dislocations in Solids*, edited by J. Hirth and L. Kubin (Elsevier, Amsterdam, 2009), Vol. 15.

[6] T. Haxhimali, D. Buta, M. Asta, P. W. Voorhees, and J. J. Hoyt, Phys. Rev. E **80**, 050601 (2009).

[7] Y. G. Zheng, H. W. Zhang, Z. Chen, C. Lu, and Y. Mai, Phys. Lett. A **373**, 0570 (2009).

[8] Y. Wang, Y. Jin, and A. Khachaturyan, Acta Mater. **49**, 1847 (2001).

[9] M. Haataja, J. Muller, A. D. Rutenberg, and M. Grant, Phys. Rev. B **65**, 165414 (2002).

[10] A. Artemev, Y. Jin, and A. Khachaturyan, Acta Mater. **49**, 1165 (2001).

[11] J. Zhu, T. Wang, A. Ardell, S. Zhou, Z. Liu, and L. Chen, Acta Mater. **52**, 2837 (2004).

[12] M. Greenwood, J. Hoyt, and N. Provatas, Acta Mater. **57**, 2613 (2009).

[13] M. Parrinello and A. Rahman, Phys. Rev. Lett. **45**, 1196 (1980).

[14] M. S. Daw and M. I. Baskes, Phys. Rev. B **29**, 6443 (1984).

[15] M. Finnis and J. Sinclair, Philos. Mag. A **50**, 45 (1984).

[16] T. V. Ramakrishnan and M. Yussouff, Phys. Rev. B **19**, 2775 (1979).

[17] C. Ebner, H. R. Krishnamurthy, and R. Pandit, Phys. Rev. A **43**, 4355 (1991).

[18] P. Tarazona and U. Marconi, J. Chem. Phys. **110**, 8032 (1999).

[19] A. Archer and M. Rauscher, J. Phys. A **37**, 9325 (2004).

[20] A. Jaatinen, C. V. Achim, K. R. Elder, and T. Ala Nissila, Phys. Rev. E **80**, 031602 (2009).

[21] K. R. Elder, M. Katakowski, M. Haataja, and M. Grant, Phys. Rev. Lett. **88**, 245701 (2002).

[22] K. R. Elder and M. Grant, Phys. Rev. E **70**, 051605 (2004).

[23] P. Stefanovic, M. Haataja, and N. Provatas, Phys. Rev. Lett. **96**, 225504 (2006).

[24] J. Berry, M. Grant, and K. R. Elder, Phys. Rev. E **73**, 031609 (2006).

[25] J. Swift and P. Hohenberg, Phys. Rev. A **15**, 319 (1977).

[26] K. R. Elder, N. Provatas, J. Berry, P. Stefanovic, and M. Grant, Phys. Rev. B **75**, 064107 (2007).

[27] J. Berry, K. R. Elder, and M. Grant, Phys. Rev. B **77**, 224114 (2008).

[28] K. Wu and A. Karma, Phys. Rev. B **76**, 184107 (2007).

[29] J. Mellenthin, A. Karma, and M. Plapp, Phys. Rev. B **78**, 184110 (2008).

[30] G. Toth, G. Tegze, T. Pusztai, G. Toth, and G. Laszlo, J. Phys. Condens. Matter **22**, 0953 (2010).

[31] A. Jaatinen and T. Ala Nissila, J. Phys. Condens. Matter **22**, 205402 (2010).

[32] K.-A. Wu, Ph.D. thesis, Northeastern University (2006).

[33] K. A. Wu, A. Adland, and A. Karma, Phys. Rev. E **81**, 061601 (2010).

[34] K. Wu, M. Plapp, and P. Voorhees, J. Phys. Condens. Matter **22**, 364102 (2010).

[35] M. Greenwood, N. Provatas, and J. Rottler, Phys. Rev. Lett. **105**, 045702 (2010).

[36] M. Cheng and J. Warren, J. Comput. Phys. **227**, 6241 (2008).

[37] N. Goldenfeld, B. P. Athreya, and J. A. Dantzig, Phys. Rev. E **72**, 020601 (2005).

[38] J. A. P. Ramos, E. Granato, C. V. Achim, S. C. Ying, K. R. Elder, and T. Ala Nissila, Phys. Rev. E **78**, 031109 (2008).

[39] J. Berry, K. R. Elder, and M. Grant, Phys. Rev. E **77**, 061506 (2008).

[40] G. Tegze, L. Granasy, G. I. Toth, F. Podmaniczky, A. Jaatinen, T. Ala Nissila, and T. Pusztai, Phys. Rev. Lett. **103**, 035702 (2009).

[41] Z. F. Huang, K. R. Elder, and N. Provatas, Phys. Rev. E **82**, 021605 (2010).

[42] N. Goldenfeld, B. Athreya, and J. Dantzig, J. Stat. Phys. **125**, 1019 (2006).

[43] S. Majaniemi and N. Provatas, Phys. Rev. E **79**, 011607 (2009).

[44] M. J. Mehl, J. E. Osburn, D. A. Papaconstantopoulos, and B. M. Klein, Phys. Rev. B **41**, 10311 (1990).

[45] M. J. Mehl, Phys. Rev. B **47**, 2493 (1993).

[46] R. Zhu, E. Pan, P. Chung, X. Cai, K. Liew, and A. Buldum, Semicond. Sci. Technol. **21**, 906 (2006).

[47] F. Birch, J. Geophys. Res. **83**, 1257 (1978).